Investigation of Radiated Electromagnetic Interference for an Isolated High-Frequency DC–DC Power Converter With Power Cables

Yingjie Zhang, *Student Member, IEEE*, Shuo Wang, *Fellow, IEEE*, and Yongbin Chu

***Abstract*—To analyze the radiated electromagnetic interference generated by isolated power converters, this paper proposes a technique to develop a general radiation model for the converters. The radiated electric field can be predicted from the developed model. The interaction between the impedance of the converter and the undesired antenna in the converter's power delivery paths is explored in detail based on the developed model. Moreover, a dual active bridge converter is taken as an example to demonstrate the developed modeling technique based on the converter's topology. The radiated electric field of the dual active bridge converter is predicted from the developed model. Experiments are conducted to validate the developed model and the predicted interaction between the converter impedance and the undesired antenna impedance in the power delivery paths.**

***Index Terms*—Cables, far-field, isolated power converters, radiated electromagnetic interference (EMI), radiation model.**

I. Introduction

Switching frequencies of power converters have been significantly increased to enhance the power density in recent years. Radiated electromagnetic interference (EMI) becomes more and more important because it is a headache issue for many high-frequency power electronics applications. The conducted EMI of power converters has been investigated in many papers [1]–[8]. On the other hand, few papers address radiated EMI for power electronics applications. EMI standards specify both conducted and radiated EMI limits. In industry applications, it is not unusual that even the conducted EMI meets the EMI standards, the radiated EMI may still be over the limits. It is, therefore, necessary to investigate radiated EMI.

To understand and analyze the radiated EMI generated from power converters, the power converter's radiation model must be first developed. The mechanisms of two radiated EMI sources were identified for a printed circuit board (PCB) with attached cables in [9]. While these two mechanisms can explain the radiated EMI noise sources, they could not be directly applied to power converter analysis. Chen *et al.* [10] analyzed a radiation model based on a buck converter. A TEM cell was used to extract the equivalent noise voltage source and the radiated electric field was simulated in a full-wave simulation software based on the physical structure of the converter. Although the model can simulate the radiated EMI, it cannot disclose the relationship between the radiated EMI and the converter.

Near-field scan was also used to develop radiation models in electromagnetic compatibility area. The basic principle is based on the theory: if two sources generate identical near field on one enclosed surface, they will have the identical radiated far field. Aouine *et al.* [11] and Beghou *et al.* [12] measured the near magnetic field generated by converters. Magnetic dipoles that can generate similar magnetic field to the measured near magnetic field are used to replace the original converters. However, in many power electronics applications, the conventional magnetic dipoles cannot generate similar near magnetic field to the measured one. Hernando *et al.* [13] and Gao *et al.* [14] applied source reconstruction technique to predict the far-field radiation based on near-field scan. The current distribution on a PCB is first derived from the scanned near magnetic field. The far-field radiation can then be calculated from the derived current distribution. Nevertheless, this technique still has big limitations in the understanding and analysis of the radiated EMI from power electronics systems as it conceals the relationship between the power electronics circuits and the radiated EMI.

This paper developed a general modeling technique for the radiated EMI of isolated power converters. The model is developed based on power converter topology and operation states. The interaction between the converter and the undesired antenna in the systems as well as its influence on the radiated EMI is analyzed using the developed model. Based on the developed model, the radiated EMI is predicted. The prediction is validated with the measured radiated EMI. This paper is organized as follows. In Section II, a general radiation model for isolated power converters is developed. Its relationship with radiated EMI and the influence of the interaction between the power converter and the undesired antenna in power delivery paths are also explored. In Section III, important parameters are experimentally extracted and a radiation model is developed for a dual active bridge (DAB) converter. Experiments are conducted in Section IV to verify the developed radiation model and the predicted interaction.

Manuscript received July 31, 2018; revised October 30, 2018; accepted December 29, 2018. Date of publication January 14, 2019; date of current version June 28, 2019. This work was supported by the Texas Instruments Inc. Recommended for publication by Associate Editor T. Shimizu. *(Corresponding author: Shuo Wang.)*

Y. Zhang and S. Wang are with the University of Florida, Gainesville, FL 32611 USA (e-mail: zhangyingjie@ufl.edu; shuowang@ieee.org).

Y. Chu is with the Texas Instruments, Inc., Dallas, TX 75243 USA (e-mail: y-chu4@ti.com).

Color versions of one or more of the figures in this paper are available online at http://ieeexplore.ieee.org.

Digital Object Identifier 10.1109/TPEL.2019.2892706

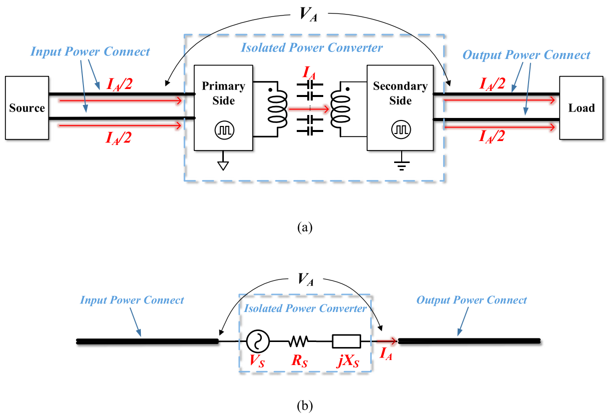

Fig. 1. Radiation mechanism of an isolated power converter. (a) CM current flowing through the parasitic capacitance between transformer windings. (b) Equivalent model.

II. General Radiation Model of Isolated Power Converters

A. Isolated Power Converter Model

The volume of power converters has been greatly reduced with increased switching frequencies, however, long power connects, such as power cables, are still needed to connect power converters to power sources, power loads, or other power converters as shown in Fig. 1(a). At the same time, transformers are used in isolated power converters to achieve galvanic isolation. High-speed semiconductor switches generate high *dv/dt* pulsating voltages on primary side, secondary side, and across two windings. It is assumed that the two conductors of the power connects on both input and output sides are balanced so they can be treated as one conductor for common mode (CM) currents. The parasitic capacitance between transformer primary and secondary windings can conduct CM currents between the two windings. Based on the Thevenin equivalence theorem, for CM EMI noise, the isolated power converter in the dash line box can be represented with an equivalent noise voltage source V_S in series with an equivalent impedance $R_s + jX_s$, as shown in Fig. 1(b). $R_s + jX_s$ represents the CM impedance of the power converter. At high frequencies, the source impedance mostly depends on the parasitic parameters of the components such as transformers, CM inductors, and PCB traces. The input and output power connects can radiate EMI like an undesired antenna and it has an impedance which is addressed in Section II-B. The equivalent voltage source V_S generates CM current I_A through $R_s + jX_s$ and the antenna impedance of input and output power connects. Different from conventional dipole antenna which has identical length for two poles and is driven by a voltage source, the input and output of power connects in the power converter may have different length and is driven by a voltage source in series with an equivalent source impedance $R_s + jX_s$.

B. Model of the Undesired Antenna

In antenna theory, the antenna impedance includes three parts: radiation resistance R_r representing the radiated power, loss resistance R_l representing ohmic power loss, and reactance jX_A

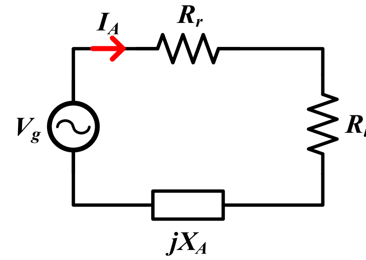

Fig. 2. Impedance model of an antenna.

representing the energy stored in near field as shown in Fig. 2. It should be pointed out that, the effects of the parasitic impedance between the cables and the ground are included in the model of antenna based on antenna theory. When the antenna is driven by a voltage source V_g, the current I_A flowing into the antenna can be calculated based on the following equation:

$$|I_A| = \frac{|V_g|}{\sqrt{(R_r + R_l)^2 + X_A^2}}. \tag{1}$$

The radiated power P_r can be derived in the following equation [15]:

$$P_r = \frac{1}{2}|I_A|^2 R_r. \tag{2}$$

The radiated power P_r can also be expressed with the total resistance R_A of the antenna

$$P_r = \frac{1}{2}e|I_A|^2 R_A \tag{3}$$

where

$$R_A = R_r + R_l \tag{4}$$

and *e* is the radiation efficiency of the antenna

$$e = \frac{R_r}{R_A}. \tag{5}$$

The maximum directivity D_o of an antenna at distance *r* is defined as the ratio of the maximum power density $S_{\max}$ at a certain direction to the average power density $P_r/(4\pi r^2)$ over a sphere as observed in the far field. It is determined by the antenna structure

$$D_o = \frac{4\pi r^2 S_{\max}}{P_r}. \tag{6}$$

$S_{\max}$ can be expressed with the maximum electric field $E_{\max}$ as

$$S_{\max} = \frac{1}{2}E_{\max}H_{\max} = \frac{1}{2}\frac{E_{\max}^2}{\eta} \tag{7}$$

where η is the intrinsic impedance of free space. From (6) and (7), $E_{\max}$ can be derived as

$$E_{\max} = \sqrt{\frac{\eta D_o P_r}{2\pi r^2}} = \sqrt{\frac{\eta e D_o}{4\pi r^2}} \times |I_A|\sqrt{R_A}$$
$$= \sqrt{\frac{\eta G_o}{4\pi r^2}} \times |I_A|\sqrt{R_A} \tag{8}$$

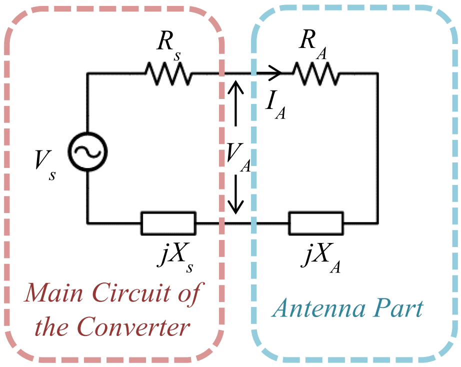

Fig. 3. General radiation model of an isolated power converter.

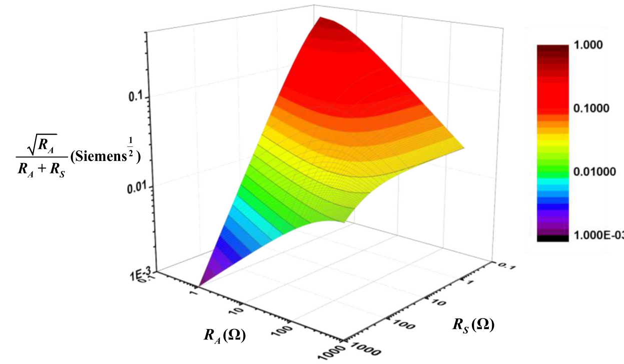

Fig. 4. Influence of resistances on $E_{\max}$.

where

$$G_o = eD_o. \tag{9}$$

In (8) and (9), G_o is the maximum gain of the antenna, which is determined by the antenna structure. In the standards of radiated EMI measurement, r could be either 3 m or 10 m [16], [17]. G_o gradually increases as the frequency increases [18]. The term $\sqrt{\eta G_o/4\pi r^2}$ in (8) is a slow changing term, therefore, it will not significantly change the profile of $E_{\max}$ within a limited frequency range. In (8), the change of $E_{\max}$ is mostly determined by $\sqrt{R_A}$ and the current I_A flowing into the antenna.

C. General Radiation Model

Based on Figs. 1(b) and 2, the general radiation model of isolated power converters is developed in Fig. 3. V_A is the excitation voltage induced on the input of the antenna.

Based on the radiation model in Fig. 3, I_A is

$$|I_A| = \frac{|V_s|}{\sqrt{(R_A+R_s)^2 + (X_A+X_s)^2}}. \tag{10}$$

And based on (8), the maximum electric field is, therefore,

$$\begin{aligned} E_{\max} &= \sqrt{\frac{\eta G_o}{4\pi r^2}} \times |I_A| \sqrt{R_A} \\ &= \sqrt{\frac{\eta G_o}{4\pi r^2}} \times \frac{|V_s| \sqrt{R_A}}{\sqrt{(R_A+R_s)^2 + (X_A+X_s)^2}}. \end{aligned} \tag{11}$$

From (10), besides the voltage source V_s, the interaction between the source impedance and the antenna impedance in the denominator can greatly affect I_A and the radiated $E_{\max}$.

D. Interactions Between Converter Source Impedance and Antenna Impedance

The two conditions of the interactions to generate high radiated EMI can be derived from (11) as follows.

1) $X_A + X_s = 0$

The peaks of radiated electric field most likely happen when there is a resonance between the antenna and the main circuit of the converter, in other words, the total reactance is zero. Then,

$$E_{\max} = \sqrt{\frac{\eta G}{4\pi r^2}} \times |V_s| \times \frac{\sqrt{R_A}}{R_A+R_s}. \tag{12}$$

2) R_A and R_s are small

When the total reactance is zero, the magnitude of $E_{\max}$ is only determined by the resistance in (12). Fig. 4 illustrates the influence of resistance based on (12). From Fig. 4, $E_{\max}$ greatly increases as resistance decreases.

Generally, the reactance of the source impedance and the antenna impedance determines the frequencies at which the radiation peaks most likely happen. And the resistance determines the magnitude of the radiated EMI at those frequencies.

Table I summarizes the possible interactions between the converter and the antenna. The resonances may lead to input current peaks and generate high-level radiated EMI, especially when the total resistance is small.

III. Radiation Model of a DAB Converter

A. Derivation of the Radiation Model

Although the general radiation model in Section II can be used to analyze the radiated EMI for power converters. To understand and analyze the effects of the power converter topology, operation, and design on radiated EMI, the radiation model should be developed based on the converter topology, operation principles, and parasitics.

A 7.2 W DAB converter in Fig. 5(a) is taken as an example in this paper for demonstrating the developed radiation models. Both input and output voltages are 12 V. The converter is powered by a battery. The switching frequency is around 700 kHz.

The DAB converter has input and output differential mode (DM) decoupling capacitors C_{in} and C_{out}. Both C_{in} and C_{out} are one 100 μF and three 0.1 μF ceramic capacitors in parallel. They have equivalent series inductance $\mathrm{ESL_{in}}$ and $\mathrm{ESL_{out}}$, and equivalent series resistance $\mathrm{ESR_{in}}$ and $\mathrm{ESR_{out}}$. The parasitic inductances of PCB traces are also shown in the figure but not labeled for concision. The parasitic parameters of MOSFETs, inductor, and transformer are not shown in the figure but they will be considered in the analysis later. The DAB converter in Fig. 5 has long input cables (AWG10) and output cables

TABLE I
INFLUENCE OF INTERACTION BETWEEN ANTENNA AND CONVERTER

Antenna	Main Circuit of Converter	Possible Effect
Series Resonance 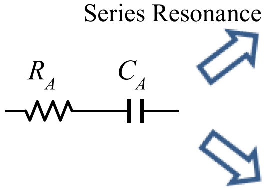	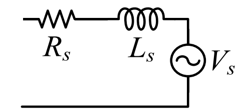	High radiated EMI may be generated at resonant frequency, especially when resistance is small
	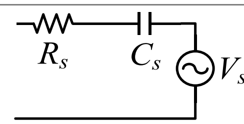	Level of radiated EMI mostly depends on the reactance and the source voltage
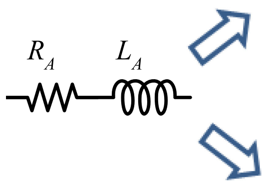 Series Resonance	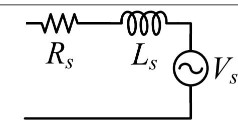	Level of radiated EMI mostly depends on the reactance and the source voltage
	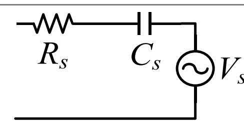	High radiated EMI may be generated at resonant frequency, especially when resistance is small

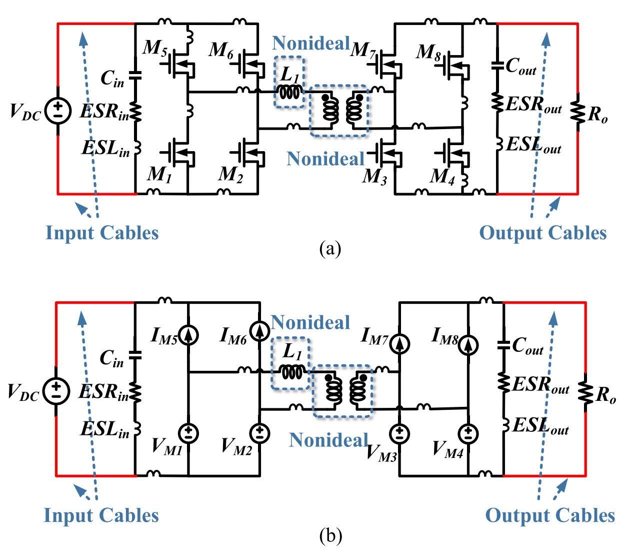

Fig. 5. DAB converter under investigation. a) Circuit. b) MOSFETs replaced with voltage and current sources based on substitution theory.

(AWG10) connected to the battery and the load, respectively. The cables behave like an undesired antenna at high frequencies. The high-frequency parasitics inside the converter will greatly affect the high-frequency characteristics of source impedance so that they cannot be ignored.

Based on the technique developed in [1], [19], and [20], in Fig. 5(b), the substitution theory is applied to the switching devices. The four low-side MOSFETS M_1–M_4 and the trace parasitics on drain and source branches are replaced with four voltage sources V_{M1}–V_{M4}, which have the same voltage waveforms as the drain to source voltages of the four MOSFETs, while the four high-side MOSFETS M_5–M_8 and the trace parasitics on drain and source branches are replaced with four current sources I_{M5}–I_{M8}, which have the same current waveforms as the drain to source currents of these four MOSFETs. The basic rules of applying substitution theory to replace nonlinear switching devices in a power electronics system for EMI analysis have been addressed in [19] and [20], so it will not be repeated here. Because the voltage and current sources have the same voltage and current waveforms as the original MOSFETs to be replaced with, they have all EMI information including that due to parasitics of the MOSFETs. The measured impedance of DM capacitors C_{in} and C_{out} is dominated by the 0.9 nH ESL_{in} and 0.9 nH ESL_{out} from 30 MHz to 1 GHz. They can be considered short circuits in radiated EMI analysis as shown in Fig. 6(a) because the measured impedances are always much smaller than the cable antenna's DM impedance and the two conductors of the input/output cables are well balanced.

Based on the superposition theory, the effects of each source on the radiated EMI can be analyzed separately. For example, the effects of current source I_{M5} can be analyzed in Fig. 6(b) with all the other current sources open and all the voltage sources shorted.

From Fig. 6(b), I_{M5} can only generate DM current in the converter so it will not flow into cables for radiated EMI generation. However, I_{M5} could contribute to the radiation of a loop antenna, but due to the small size of the current loop, the generated radiated electric field can always be ignored compared with that radiated from the input and output cables [21]. The noise models of all the other current sources are similar, therefore, the current sources do not contribute to radiated EMI.

The effects of the voltage source V_{M1} can be analyzed in Fig. 6(c). Because of the CM parasitics between the primary and secondary windings, CM current can be generated and flow from the converter to the cable antenna. V_{M1}, therefore, contributes to radiated EMI. The noise models of all the other voltage sources are similar, so the analysis will not be repeated here.

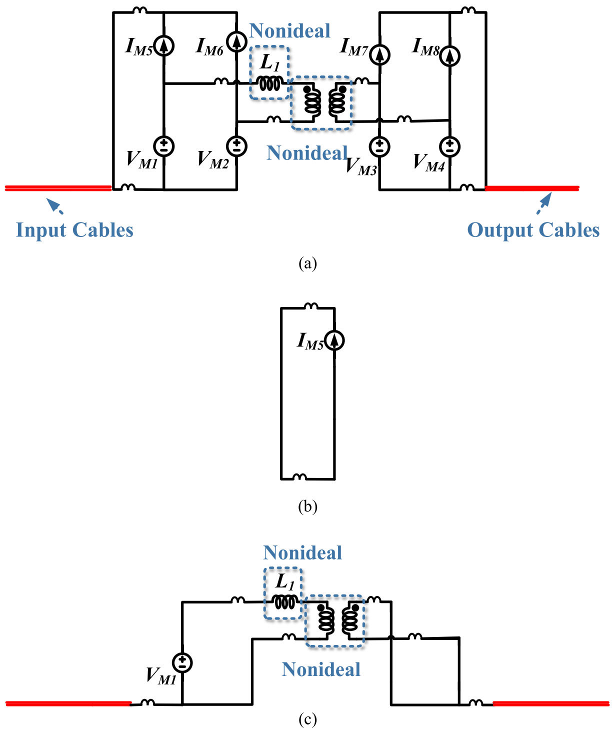

Fig. 6. (a) Radiation model for a DAB converter. (b) Noise model of I_{M5}. (c) Noise model of V_{M1}.

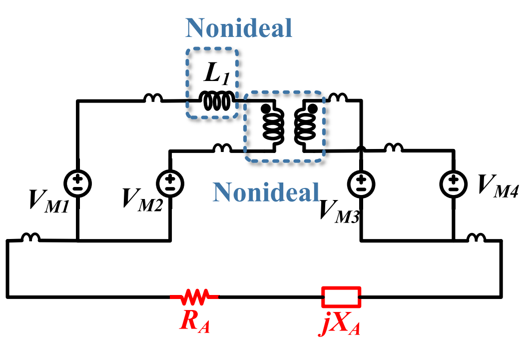

Fig. 7. Simplified radiation model for DAB converter.

In conclusion, the radiated EMI is dominantly generated by equivalent noise voltage sources. Hence, the current sources can be ignored and replaced with open circuit based on the superposition theory. According to the previous analysis, the input cables and output cables can be represented with the antenna model $R_A + jX_A$. As a result, the final radiation model of the DAB converter is shown in Fig. 7.

Following the same rule, the developed technique can also be applied to other isolated power converters, e.g., the radiation models of a flyback converter, a full-bridge converter, and a half-bridge *LLC* converter can be developed, as shown in Figs. 8, 9, and 10, respectively.

B. Extraction of Parameters

The parameters of the transformer, inductor, and PCB traces need to be extracted appropriately for the model in Fig. 7 so it can be analyzed and used to predict the radiated EMI. The experiment is conducted as shown in Fig. 11.

The impedance of the antenna includes the input cables, the battery, the output cables, and a small-size load resistor. Because the battery size is huge with a complicated structure, making it difficult to evaluate the influence of cables, in experiments, six ferrite beads are added at the end of input cables before the battery to provide high impedance in the concerned frequency range. Therefore, the battery can be isolated from the input cables. These six ferrite beads and their impedance are: two HFA259131-0A2 (250 Ω@300 MHz, 315 Ω@500 MHz, 272 Ω@800 MHz, 200 Ω@1 GHz), two 28A3851-0A2 (150 Ω@25 MHz, 260 Ω@100 MHz, 410 Ω@300 MHz), and two TX36/23/15-4C65 (43 Ω@25 MHz, 111 Ω@100 MHz, 468 Ω@300 MHz, 94 Ω@1 GHz). Consequently, the battery is no longer part of the antenna and its influence on the radiated electric field can be ignored. The effective length (32 cm) of the input cables is, therefore, equal to the distance between the ferrite beads and the circuit board. The length of output cables is 39 cm.

The impedance of the antenna was measured with DAB converter board removed in Fig. 12. The battery was disconnected from the input cables, while the load resistor was still connected to the output cables. The two conductors of both the input and output cables are shorted at the ends close to the DAB board because of the small impedances of C_{in} and C_{out} as analyzed previously. Finally, the impedance was measured using a Copper Mountain PLANAR 808/1 vector network analyzer (VNA), as shown in Fig. 12 in a fully anechoic chamber, while the distance between the cables and the ground is 80 cm. The measured result is shown in Fig. 13.

In Fig. 13, zero phase happens around 178 MHz, corresponding to 0.48 λ while the length of the antenna is 0.81 m. The antenna's impedance changes from capacitive to inductive at this frequency. This agrees with the antenna theory.

Based on the radiation model of the DAB converter in Fig. 7, the superposition theory is employed to analyze the induced excitation voltages added to the cable antenna due to four voltage sources V_{M1}, V_{M2}, V_{M3}, and V_{M4}. Based on the superposition theory, the four radiation models are shown in Fig. 14.

In Fig. 14, the four voltage sources V_{M1}, V_{M2}, V_{M3}, V_{M4} induce excitation voltages V_{A1}, V_{A2}, V_{A3}, V_{A4} on the antenna, respectively. Based on the superposition theory, the total excitation voltage V_A is the sum of V_{A1}–V_{A4}. Because the four radiation models are similar, only the radiation model of V_{M1} will be analyzed here.

The time-domain waveform of MOSFET M_1's drain to source voltage V_{M1} can be measured with a wideband oscilloscope: Rigol MSO4054 (500 MHz bandwidth). Since the input impedance of the probe is very high at 1 MΩ, the probe will not greatly affect the measured voltage. The measured voltage waveform is shown in Fig. 15(a). The spectrum of V_{M1} was derived from the time-domain waveform via fast Fourier transform in Fig. 15(b).

Because within the radiated EMI frequency range, the CM current flows from the primary winding to the secondary winding through the parasitics such as the leakage inductances and

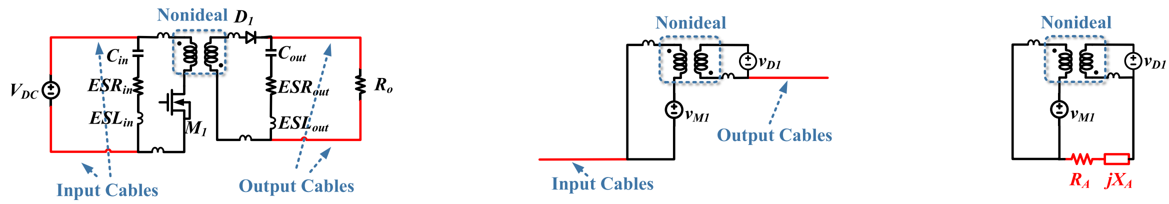

(a) (b) (c)

Fig. 8. Radiation model of a flyback converter. (a) Converter circuit. (b) Substituting nonlinear devices with voltage and current sources. (c) Final radiation model.

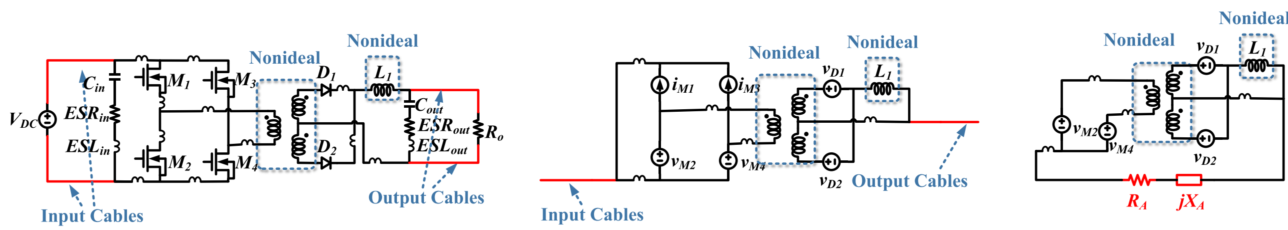

(a) (b) (c)

Fig. 9. Radiation model of a full-bridge converter. (a) Converter circuit. (b) Substituting nonlinear devices with voltage and current sources. (c) Final radiation model.

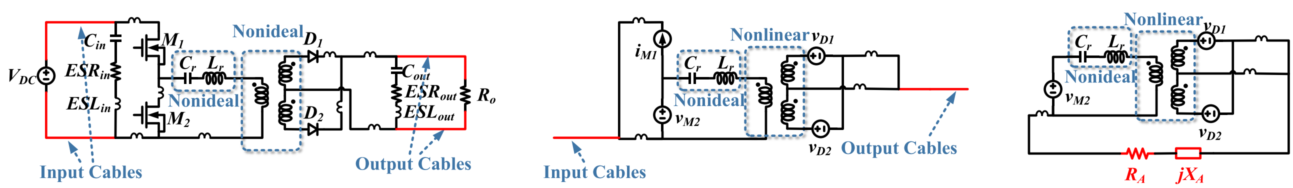

(a) (b) (c)

Fig. 10. Radiation model of a half-bridge *LLC* converter. (a) Converter circuit. (b) Substituting nonlinear devices with voltage and current sources. (c) Final radiation model.

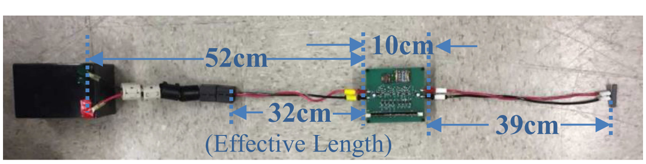

Fig. 11. Prototype of the DAB converter.

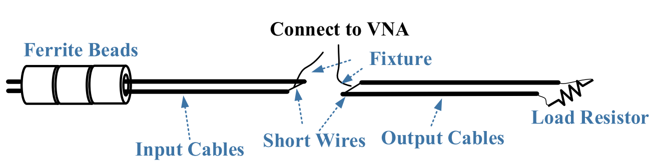

Fig. 12. Measurement setup for antenna impedance measurement.

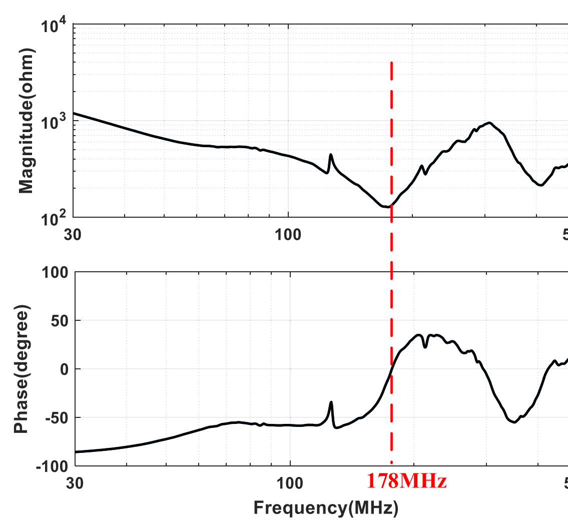

Fig. 13. Measured impedance of the antenna.

the winding capacitance between the primary and the secondary windings and these parasitics are not a function of CM currents, the voltage gain VG_1 from V_{M1} to V_{A1} can be extracted with small signal measurement.

From the radiation model of V_{M1} in Fig. 14(a), the passive components and PCB traces between V_{M1} and the antenna can be considered as a two-port network in Fig. 16(a). Port 1 is connected to V_{M1} and port 2 is connected to antenna. The voltage gain VG_1 from V_{M1} to V_{A1} in the following equation can be extracted using *S*-parameters in Fig. 16(b):

$$VG_1 = \frac{V_{A1}}{V_{M1}}. \tag{13}$$

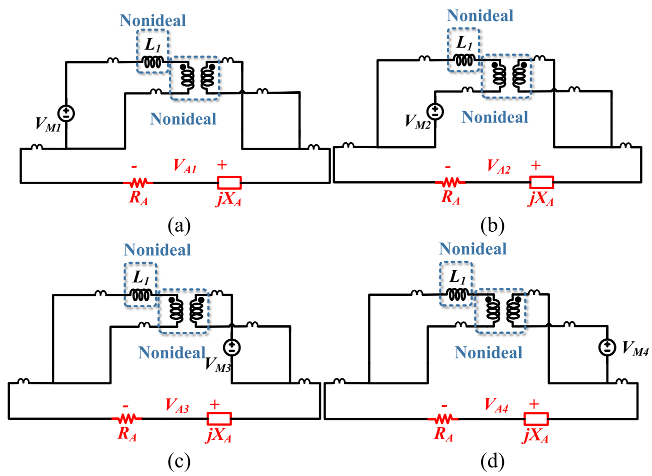

Fig. 14. Radiation model due to each equivalent voltage source. (a) V_{M1}. (b) V_{M2}. (c) V_{M3}. (d) V_{M4}.

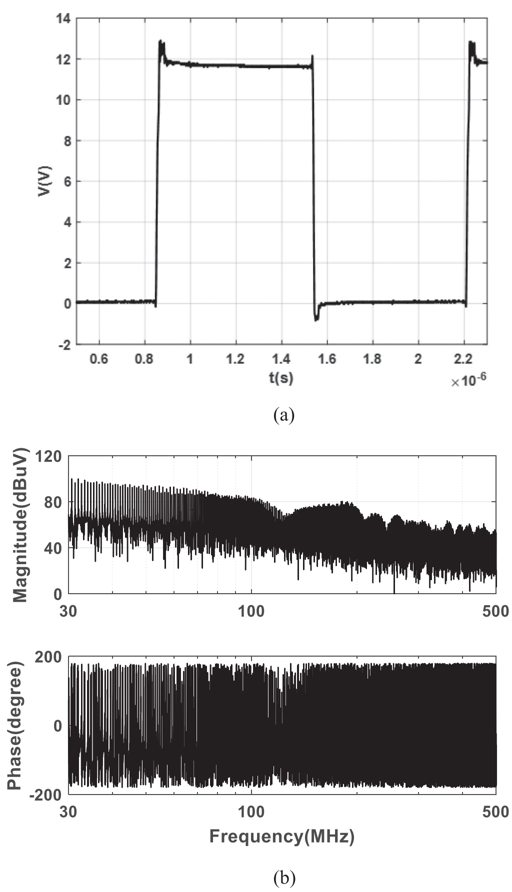

Fig. 15. Develop radiation model for V_{M1}. (a) Measured time domain waveform of V_{M1}. (b) Spectrum.

To perform a two-port S-parameter measurement, the cable antenna is first removed. Next, three low-side MOSFETs M_2–M_4 are shorted and four high-side MOSFETs M_5–M_8 are removed according to the superposition theory. M_1 is removed and replaced with the port 1 of the VNA and the port 2 of VNA is added between the input and output where the antenna was originally connected to.

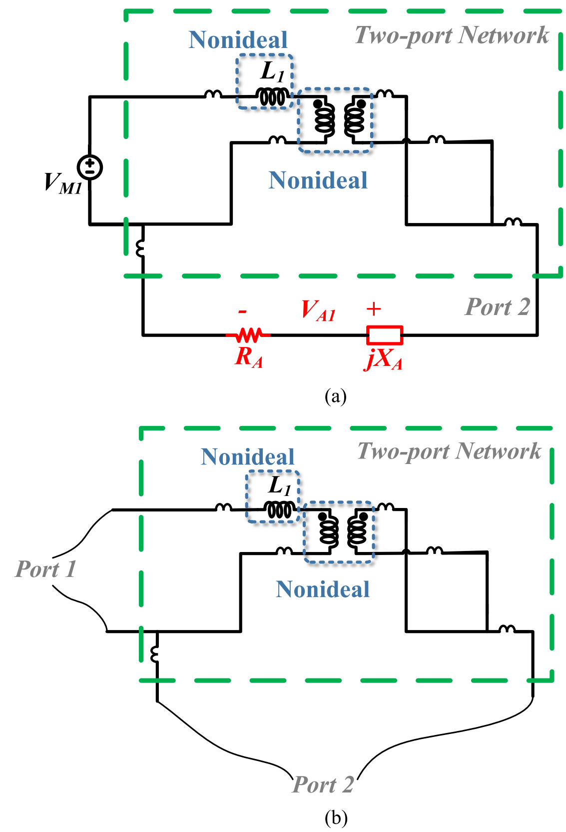

Fig. 16. Developing radiation model for V_{M1}. (a) Two port network to find voltage gain. (b) Measurement setup for S-parameters.

VG_1 can be calculated from the measured S-parameters as follows [22], [23]:

$$VG_1 = \frac{S_{21}(1+\Gamma_A)}{(1+S_{11})(1-S_{22}\Gamma_A)+S_{12}S_{21}\Gamma_A} \tag{14}$$

where Γ_A is the reflection coefficient of the antenna, which is calculated from the measured antenna impedance from the following equation:

$$\Gamma_A = \frac{R_A + jX_A - Z_o}{R_A + jX_A + Z_o} \tag{15}$$

where Z_o is the 50 Ω characteristic impedance of the VNA. The derived VG_1 based on the measured S-parameters is shown in Fig. 17.

Based on Fig. 15(b), (13)–(15), V_{A1} can be derived in Fig. 18.

Similarly, V_{M2}, V_{M3}, and V_{M4} can be measured using an oscilloscope. The voltage gains VG_2, VG_3, and VG_4 from V_{M2}, V_{M3}, and V_{M4} to V_{A2}, V_{A3}, and V_{A4} can be extract and calculated separately. Based on the superposition theory, the total excitation voltage of the antenna is given by (16) and shown in Fig. 19. Due to the bandwidth limitation of the oscilloscope, the spectrums can only be derived below 500 MHz

$$\begin{aligned} V_A &= V_{A1} + V_{A2} + V_{A3} + V_{A4} \\ &= V_{M1} \times VG_1 + V_{M2} \times VG_2 + V_{M3} \times VG_3 \\ &\quad + V_{M4} \times VG_4. \end{aligned} \tag{16}$$

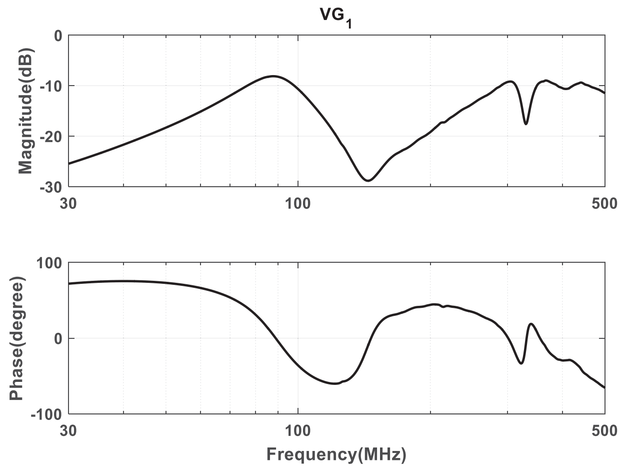

Fig. 17. Extracted VG_1 based on the measured *S*-parameters.

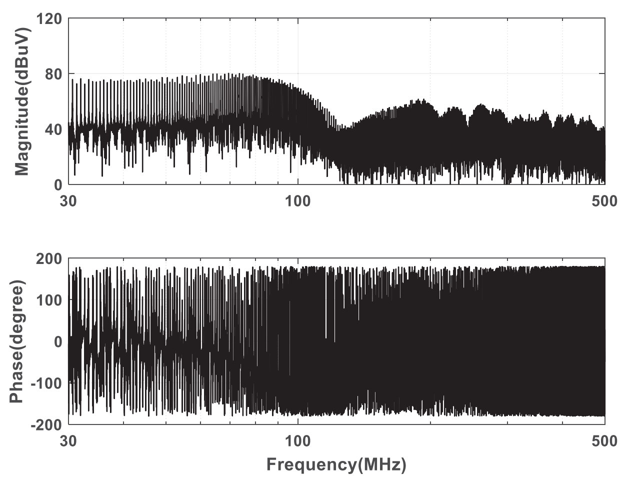

Fig. 18. Extracted V_{A1} based on the extracted VG_1 and V_{M1} spectrum.

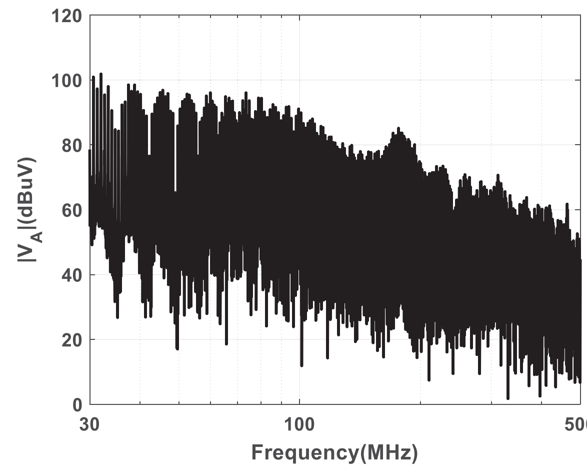

Fig. 19. Magnitude of the extracted V_A.

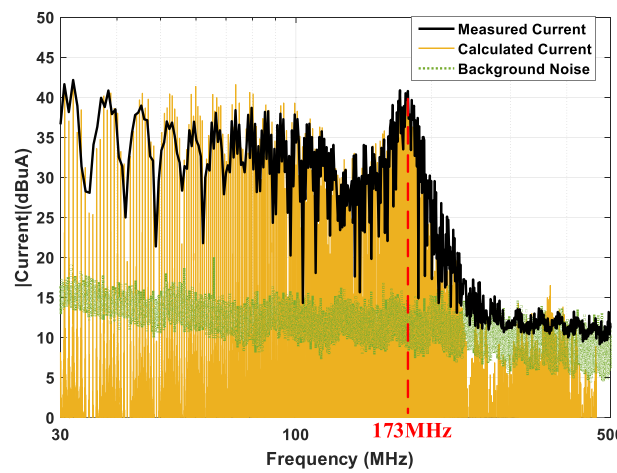

Fig. 20. Comparison of the measured and predicted CM current I_A.

The CM current I_A flowing into the antenna can be calculated in (17) based on Fig. 4 and will be shown in the Section IV compared with the directly measured CM current on the cable antenna

$$|I_A| = \frac{|V_A|}{\sqrt{R_A^2 + X_A^2}}. \tag{17}$$

IV. Experimental and Simulation Verification

A. Prediction of Radiated Electric Field

The CM current I_A flowing into the antenna can be calculated based on Figs. 13 and 19. It is compared with the directly measured CM current in Fig. 20. The CM current flowing into the cables was measured using wideband current probe ETS Lindgren 94111-1 at the cable ends close to the DAB board. The CM currents on both input and output cables are measured and they are equal so only the result from input cables is shown in Fig. 20.

In Fig. 20, the directly measured CM current matches the predicted one based on the developed model. There is only up to several dB difference from 45 to 90 MHz. The background noise of the measurement is also shown in the figure. Above 250 MHz, the CM currents are below background noise.

In order to predict the radiated electric field $E_{\max}$ based on (11), the gain G_o of the antenna is obtained from a full-wave simulation based on the physical structure of the input and output cables in Ansys HFSS. The simulated G_o is shown in Fig. 21(a). The distance r between the DAB board and the location of the concerned $E_{\max}$ is 3 m.

$E_{\max}$ is finally calculated from the antenna gain G_o and the derived I_A in Fig. 20 based on (11). It is compared with the directly measured electric field result in a 3 m fully anechoic chamber in Fig. 21(b). The electric field measurement setup is shown in Fig. 22.

From Fig. 21(b), the calculated radiated electric field $E_{\max}$ matches the measured one. There is only up to several dB difference. Therefore, the developed radiation model and equations to predict the radiated electric field are valid.

To further verify the predicted modeling technique under DAB converter's different operating conditions, the phase shift between the primary side and secondary side of the DAB is adjusted so that the output voltage is 15 V as shown in Fig. 23. The CM current I_A flowing into the antenna and the radiated

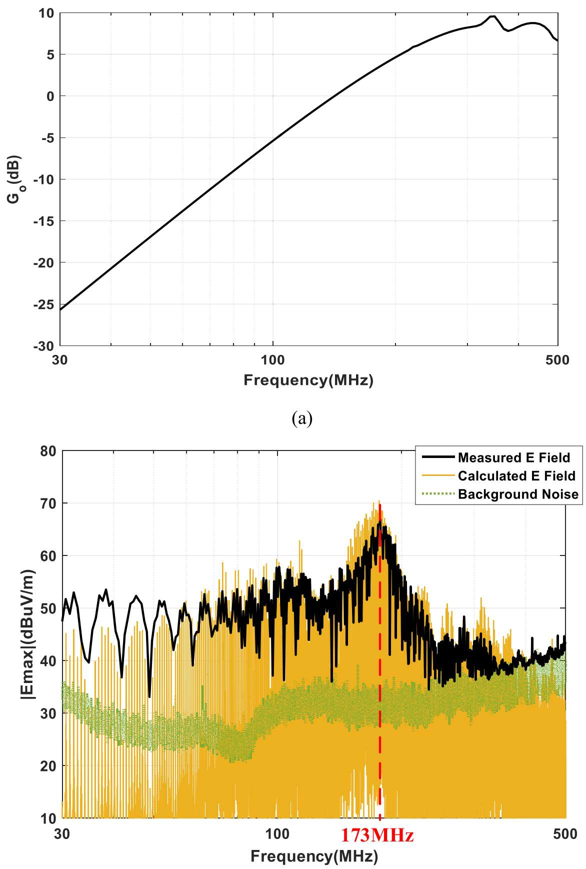

Fig. 21. (a) Simulated gain of the cable antenna. (b) Comparison of measured and calculated $E_{\max}$.

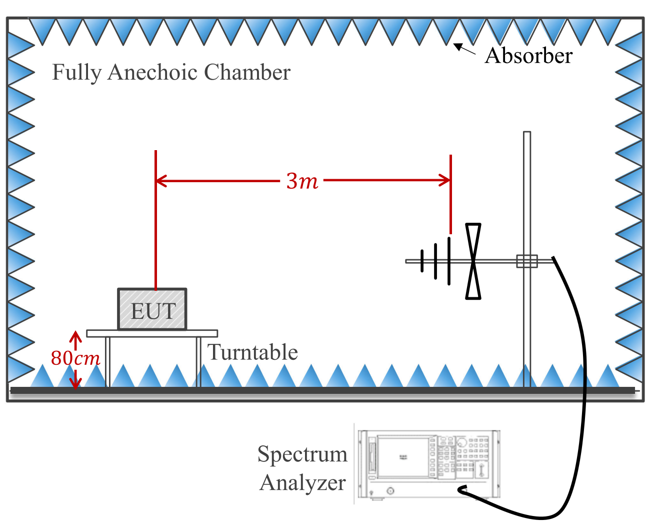

Fig. 22. Electric field measurement setup in a 3 m fully anechoic chamber.

electric field $E_{\max}$ are predicted in the same way as described previously and compared with the measured results in Fig. 24.

From Fig. 24, the calculated CM current I_A and radiated electric field $E_{\max}$ match the measured results. Consequently, the radiation model and the equations to predict the radiated electric field are verified under different operating conditions.

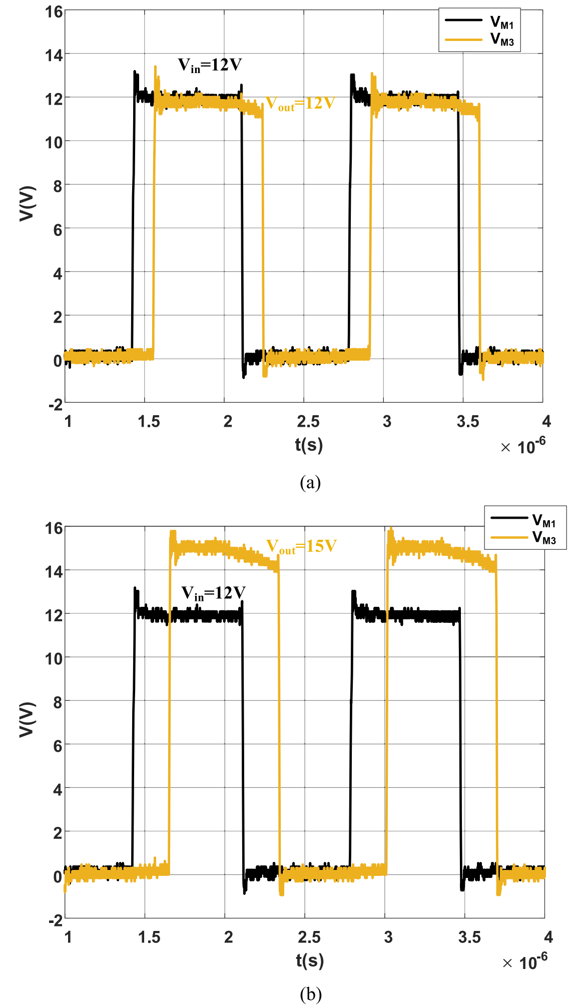

Fig. 23. Time domain waveform of V_{M1} and V_{M3}. (a) When output voltage is 12 V (7.2 W). (b) When output voltage is 15 V (11.3 W).

B. Effect of Interaction Between the Converter and the Cable Antenna

Based on pervious analysis, the impedance interaction between the converter and the antenna will affect the radiated electric field. To verify it, the equivalent source impedance of the converter is first extracted with a Copper Mountain PLANAR 808/1 VNA with the cables disconnected. Based on the Thevenin equivalence theorem, when measuring the output impedance of a network, all voltage sources in the network should be shorted and all current sources in the network should be open. Because of this, in Fig. 5(b), the four low-side MOSFETs M_1–M_4 are shorted and four high-side MOSFETs M_5–M_8 are removed in the measurement. The measured output impedance of the converter is analyzed with the measured antenna impedance in the terms of resistance, the magnitude of reactance, and the phase of reactance in Fig. 25.

As analyzed in Section II-D, the high radiated electric field likely happens when the antenna impedance resonates with the converter output impedance because the resonance causes zero reactance and may lead to low impedance in the impedance loop of Fig. 3. From Fig. 25, there are three resonant frequencies

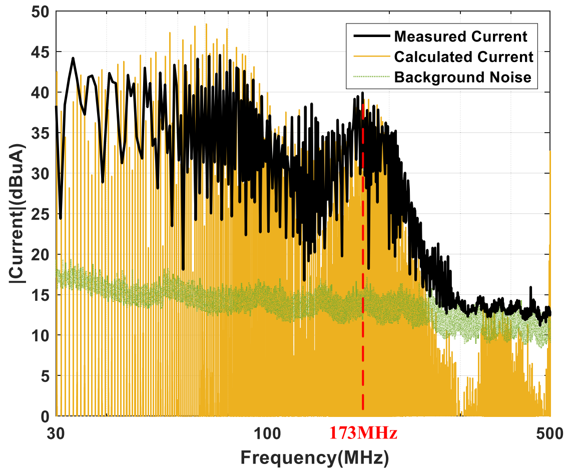

(a)

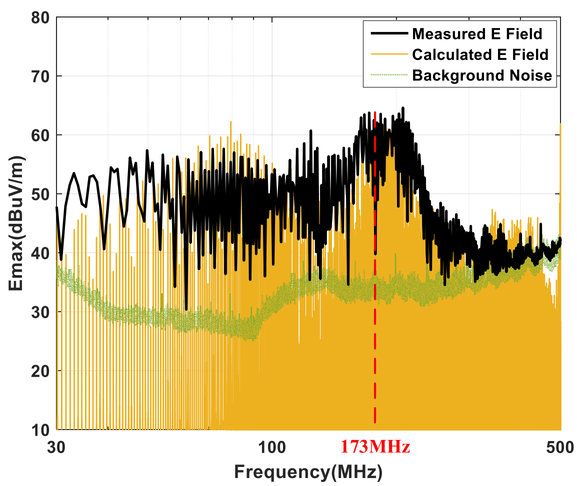

(b)

Fig. 24. Comparison of the calculated and measured. (a) CM current I_A. (b) $E_{\max}$ when the output voltage of the DAB converter is 15 V (11.3 W).

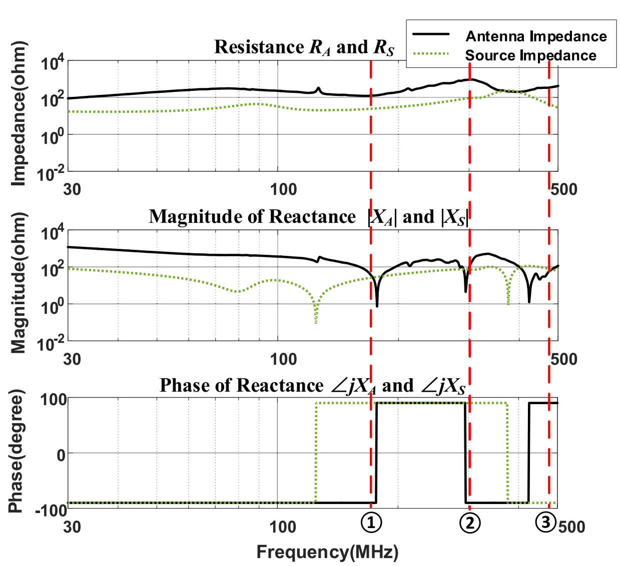

Fig. 25. Interaction of converter source impedance and cable antenna impedance.

TABLE II
INFLUENCE OF RESISTANCE AT RESONANT FREQUENCIES

No.	Resonant Frequency (MHz)	R_s (Ω)	R_A (Ω)	K_I (S)	K_E ($S^{1/2}$)
①	173	24	125	0.0067	0.0750
②	301	91	910	0.0010	0.0301
③	478	42	344	0.0026	0.0480

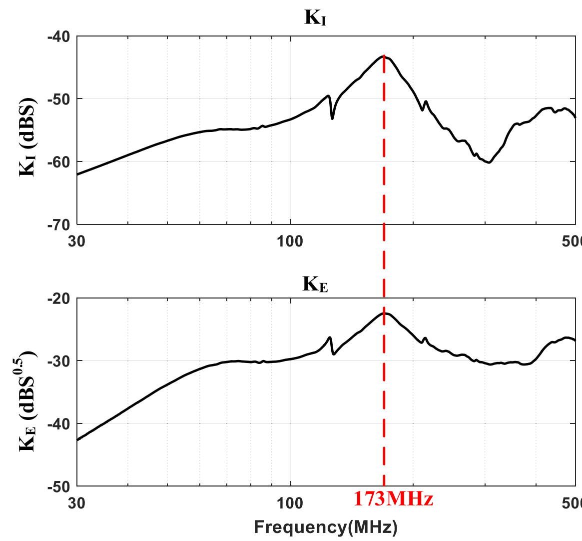

Fig. 26. Effects of interactions on CM current I_A and radiated EMI.

between 30 and 500 MHz as the reactance X_A from antenna and X_S from source impedance cancel each other at these frequencies. However, not all of them will generate radiated EMI spikes since the resistance will determine the magnitude of radiated EMI at resonant frequencies.

If K_I represents the influence of the interactions between the converter source impedance and antenna impedance to the current I_A and K_E represents the influence of the interactions to the radiated electric field $E_{\max}$, from (10) and (11), (18) and (19) can be derived to represent the influence of the interactions to CM current I_A and electric field $E_{\max}$. K_I and K_E are given by (20) and (21), respectively. Table II lists all the resonant frequencies, corresponding resistances, and the coefficient K_I and K_E based on Fig. 25. In addition, the curves of K_I and K_E are also plotted in Fig. 26

$$|I_A| = |V_s|\, K_I \tag{18}$$

$$E_{\max} = \sqrt{\frac{\eta G_o}{4\pi r^2}} \times |V_s|\, K_E \tag{19}$$

$$K_I = \frac{1}{\sqrt{(R_A + R_s)^2 + (X_A + X_s)^2}} \tag{20}$$

$$K_E = \frac{\sqrt{R_A}}{\sqrt{(R_A + R_s)^2 + (X_A + X_s)^2}}. \tag{21}$$

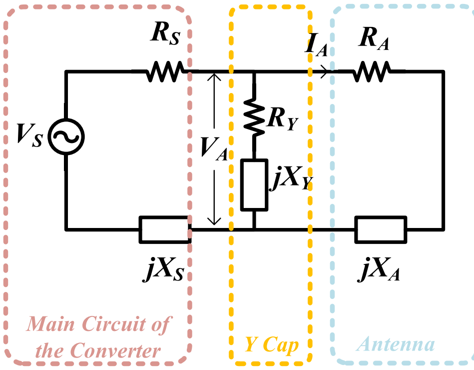

Fig. 27. Radiation model for an isolated converter with a Y-cap.

From Table II and Fig. 26, the source resistance R_S and the antenna resistance R_A are the smallest at the first resonant frequency: 173 MHz. Therefore, the highest K_I and K_E are at 173 MHz, as validated in Fig. 26. Based on the spectrum of CM current I_A in Figs. 20 and 24(a) and the radiated electric field $E_{\max}$ in Figs. 21(b) and 24(b), the peaks also show up at 173 MHz. This further verified the analysis. For the other two resonant frequencies at 301 MHz and 478 MHz, because R_S and R_A are big, both CM current and electric field have no peaks.

C. Reduction of Radiated EMI

According to the radiation model and equations of radiated electric field derived in this paper, the techniques to reduce the radiation can be derived. From (11), the radiated electric field $E_{\max}$ is directly proportional to the CM current I_A flowing into the antenna. Therefore, if the input voltage V_A on the antenna can be reduced, the CM current I_A will be reduced at the same time and the radiated electric field $E_{\max}$ will be suppressed.

To reduce V_A, a small capacitor (Y-cap) is added between the primary ground and the secondary ground in Fig. 1(a), and the radiation model with the Y-cap is illustrated in Fig. 27. R_Y is the resistance of the Y-cap, while jX_Y is its reactance. The voltage V_{A_new} across the antenna can be represented as

$$V_{A\_\text{new}} = V_S \times \frac{Z_Y||Z_A}{Z_Y||Z_A + Z_S} \tag{22}$$

where

$$Z_A = R_A + jX_A \tag{23}$$

$$Z_S = R_S + jX_S \tag{24}$$

$$Z_Y = R_Y + jX_Y. \tag{25}$$

While the voltage V_A across the antenna without the Y-cap is

$$V_A = V_S \times \frac{Z_A}{Z_A + Z_S}. \tag{26}$$

From (22) and (26), if the impedance of the Y-cap is much smaller than that of the antenna, the input voltage of the antenna can be reduced, and the radiated electric field will decrease.

To verify this, a 220 pF Y-cap is connected the primary and secondary sides. Its impedance is compared with the antenna's impedance in Fig. 28.

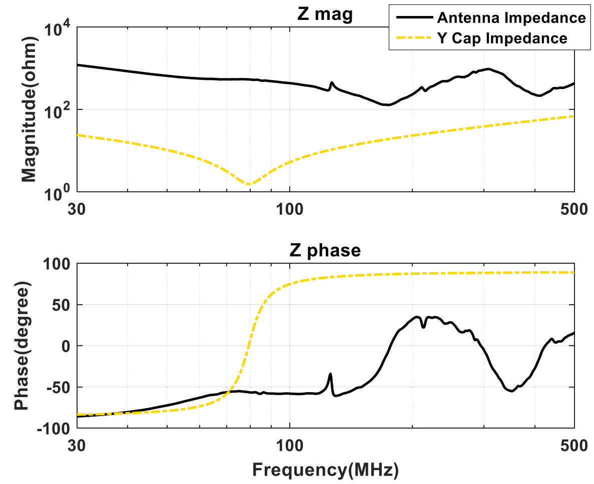

Fig. 28. Comparison of antenna's impedance and the impedance of the Y-cap.

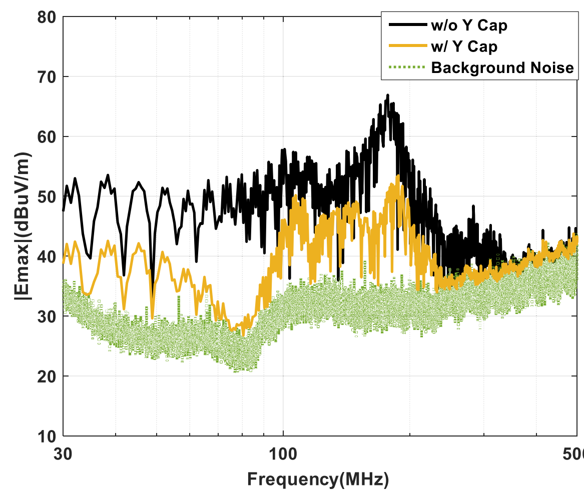

Fig. 29. Comparison of the radiated electric field $E_{\max}$ with and without the Y-cap.

And the measured radiated electric field with the Y-cap is compared with the one without the Y-cap in Fig. 29.

From Fig. 29, the radiated electric field is reduced by adding a small Y-cap, which validates the analysis.

Similarly, adding a CM inductor with impedance much higher than the antenna's impedance to either the input or output of the converter in Fig. 1(a) can also reduce V_A and the radiation.

V. Conclusion and Future Work

In this paper, a general radiation model including an isolated DC/DC converter and the undesired cable antenna was first proposed. The interaction between the converter and the cable antenna was analyzed. A DAB converter was investigated. The technique of extracting radiation model for the isolated converter was developed. The developed technique can successfully predict the radiated CM current and radiated electric field for an isolated DC/DC power converter. The interaction between the converter and the cable antenna was successfully predicted based on the developed radiation model. High radiated electric field was identified based on the model. The radiation reduction technique is also analyzed based on the model. Experiments were conducted to validate the developed technique and the model. The developed technique can be applied to other power converter topologies under different environments.

More research will be conducted based on the developed model in future papers. The relationship of source impedance to transformer parasitics will be investigated. The technique for the reduction of radiated EMI will be further explored.

References

[1] H. Zhang, L. Yang, S. Wang, and J. Puukko, "Common-mode EMI noise modeling and reduction with balance technique for three-level neutral point clamped topology," *IEEE Trans. Ind. Electron.*, vol. 64, no. 9, pp. 7563–7573, Sep. 2017.

[2] H. Akagi and T. Shimizu, "Attenuation of conducted EMI emissions from an inverter-driven motor," *IEEE Trans. Power Electron.*, vol. 23, no. 1, pp. 282–290, Jan. 2008.

[3] S. Wang and F. C. Lee, "Investigation of the transformation between differential-mode and common-mode noises in an EMI filter due to unbalance," *IEEE Trans. Electromagn. Compat.*, vol. 52, no. 3, pp. 578–587, Aug. 2010.

[4] S. Wang, F. C. Lee, and W. G. Odendaal, "Single layer iron powder core inductor model and its effect on boost PFC EMI noise," in *Proc. IEEE 34th Annu. Power Electron. Specialist Conf.*, 2003, vol. 2, pp. 847–852.

[5] D. Jiang, R. Lai, F. Wang, F. Luo, S. Wang, and D. Boroyevich, "Study of conducted EMI reduction for three-phase active front-end rectifier," *IEEE Trans. Power Electron.*, vol. 26, no. 12, pp. 3823–3831, Dec. 2011.

[6] S. Wang, Y. Y. Maillet, F. Wang, R. Lai, F. Luo, and D. Boroyevich, "Parasitic effects of grounding paths on common-mode EMI filter's performance in power electronics systems," *IEEE Trans. Ind. Electron.*, vol. 57, no. 9, pp. 3050–3059, Sep. 2010.

[7] S. Wang, F. C. Lee, and J. D. V. Wyk, "Inductor winding capacitance cancellation using mutual capacitance concept for noise reduction application," *IEEE Trans. Electromagn. Compat.*, vol. 48, no. 2, pp. 311–318, May 2006.

[8] Z. Wang, S. Wang, P. Kong, and F. C. Lee, "DM EMI noise prediction for constant on-time, critical mode power factor correction converters," *IEEE Trans. Power Electron.*, vol. 27, no. 7, pp. 3150–3157, Jul. 2012.

[9] D. M. Hockanson, J. L. Drewniak, T. H. Hubing, T. P. V. Doren, S. Fei, and M. J. Wilhelm, "Investigation of fundamental EMI source mechanisms driving common-mode radiation from printed circuit boards with attached cables," *IEEE Trans. Electromagn. Compat.*, vol. 38, no. 4, pp. 557–566, Nov. 1996.

[10] H. L. Chen, T. Wang, L. M. Feng, and G. Z. Chen, "Determining far-field EMI from near-field coupling of a power converter," *IEEE Trans. Power Electron.*, vol. 29, no. 10, pp. 5257–5264, Oct. 2014.

[11] O. Aouine, C. Labarre, and F. Costa, "Measurement and modeling of the magnetic near field radiated by a buck chopper," *IEEE Trans. Electromagn. Compat.*, vol. 50, no. 2, pp. 445–449, May 2008.

[12] L. Beghou, F. Costa, and L. Pichon, "Detection of electromagnetic radiations sources at the switching time scale using an inverse problem-based resolution method—Application to power electronic circuits," *IEEE Trans. Electromagn. Compat.*, vol. 57, no. 1, pp. 52–60, Feb. 2015.

[13] M. M. Hernando, A. Fernandez, M. Arias, M. Rodriguez, Y. Alvarez, and F. Las-Heras, "EMI radiated noise measurement system using the source reconstruction technique," *IEEE Trans. Ind. Electron.*, vol. 55, no. 9, pp. 3258–3265, Sep. 2008.

[14] X. Gao, J. Fan, Y. Zhang, H. Kajbaf, and D. Pommerenke, "Far-Field prediction using only magnetic Near-Field scanning for EMI Test," *IEEE Trans. Electromagn.Compat.*, vol. 56, no. 6, pp. 1335–1343, Dec. 2014.

[15] C. A. Balanis, *Antenna Theory: Analysis and Design*, 3rd ed. Hoboken, NJ, USA: Wiley, 2016.

[16] *FCC 47 CFR Part 15 Subpart B*, Cornell Law School, Ithaca, NY, USA, 2015.

[17] *Information Technology Equipment—Radio Disturbance Characteristics—Limits and Methods of Measurement*, CEI Standard EN 55022, 2012.

[18] W. L.Stutzman and G. A. Thiele, *Antenna Theory and Deisgn*, 3rd ed. Hoboken, NJ, USA: Wiley, 2012.

[19] S. Wang, P. Kong, and F. C. Lee, "Common mode noise reduction for boost converters using general balance technique," *IEEE Trans. Power Electron.*, vol. 22, no. 4, pp. 1410–1416, Jul. 2007.

[20] Y. Chu and S. Wang, "A generalized common-mode current cancelation approach for power converters," *IEEE Trans. Ind. Electron.*, vol. 62, no. 7, pp. 4130–4140, Jul. 2015.

[21] C. R. Paul, "A comparison of the contributions of common-mode and differential-mode currents in radiated emissions," *IEEE Trans. Electromagn. Compat.*, vol. 31, no. 2, pp. 189–193, May 1989.

[22] S. Wang, F. C. Lee, and W. G. Odendaal, "Characterization and parasitic extraction of EMI filters using scattering parameters," *IEEE Trans. Power Electron.*, vol. 20, no. 2, pp. 502–510, Mar. 2005.

[23] S. Wang, F. C. Lee, and W. G. Odendaal, "Using scattering parameters to characterize EMI filters," in *Proc. IEEE 35th Annu. Power Electron. Specialists Conf.*, 2004, vol. 1, pp. 297–303.

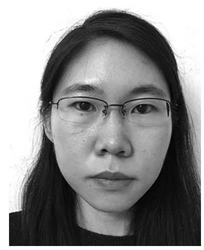

Yingjie Zhang (S'18) received the B.S.E.E. and M.S.E.E. degrees from the Huazhong University of Science and Technology, Wuhan, China, in 2013 and 2015, respectively. She is currently working toward the Ph.D. degree at the University of Florida, Gainesville, FL, USA.

Her research interests include electromagnetic interference in power converters.

Shuo Wang (S'03–M'06–SM'07-F'19) received the Ph.D. degree in electrical engineering from Virginia Tech, Blacksburg, VA, USA, in 2005.

He has been an Associate Professor with the Department of Electrical and Computer Engineering, University of Florida, Gainesville, FL, USA, since 2015. From 2010 to 2014, he was with the University of Texas at San Antonio, San Antonio, TX, USA, first as an Assistant Professor and later as an Associate Professor. From 2009 to 2010, he was a Senior Design Engineer with the GE Aviation Systems, Vandalia, OH, USA. From 2005 to 2009, he was a Research Assistant Professor with the Virginia Tech.

Dr. Wang has authored or coauthored more than 170 IEEE journal and conference papers and holds eight U.S. patents. He was the recipient of the Best Transaction Paper Award from the IEEE Power Electronics Society in 2006 and two William M. Portnoy Awards for the papers published in the IEEE Industry Applications Society in 2004 and 2012, respectively, and in 2012, the prestigious National Science Foundation CAREER Award. He is currently an Associate Editor for the IEEE Transactions on Industry Applications and a technical program Co-Chair for the IEEE 2014 International Electric Vehicle Conference.

Yongbin Chu received the B.S.E.E degree from the Hefei University of Technology, Hefei, China, in 2011 and the Ph.D. degree from the University of Texas at San Antonio, San Antonio, TX, USA, in 2015.

Since 2016, he has been with Texas Instruments Kilby Labs, Dallas, TX, USA. His research interests include electromagnetic interference/compatibility (EMI/EMC) in power electronics systems, high-efficiency and high-power-density power conversion, and circuit topologies for power electronics.

Dr. Chu has authored or coauthored more than 15 IEEE journal and conference papers.